ELSEVIER

Materials Characterization 55 (2005) 66–74

MATERIALS CHARACTERIZATION

# Evolution of dislocation density and character in hot rolled titanium determined by X-ray diffraction

I.C. Dragomir[a,*], D.S. Li[a], G.A. Castello-Branco[b,c], H. Garmestani[a], R.L. Snyder[a], G. Ribarik[d], T. Ungar[d]

[a]*School of Materials Science and Engineering, Georgia Institute of Technology, 771 Ferst Drive, N.W., Atlanta, GA 30332-0245, United States*
[b]*Department of Mechanical Engineering, Florida State University, Tallahassee, FL 32310, United States*
[c]*Centro Federal de Educacao Tecnologica, CSF-RJ, Rio de Janeiro, RJ 22710, Brazil*
[d]*Department of General Physics, Eötvös University Budapest, H-1518, P.O.B. 32, Budapest, Hungary*

Received 3 January 2005; accepted 1 March 2005

**Abstract**

X-ray Peak Profile Analysis was employed to determine the evolution dislocation density and dislocations type in hot rolled commercially pure titanium specimens. It was found that $\langle a \rangle$ dislocation type is dominating the deformation mechanism at all rolling reduction levels studied here. A good agreement was found between the texture evolution and changes in dislocation slip system activity during the deformation process.


*Keywords:* α-Titanium; X-ray line broadening; Dislocations; Burgers Vector Population; Texture

## 1. Introduction

Titanium and titanium alloys are used in a wide variety of aerospace, energy and biomedical applications, since they have very attractive properties, such as high specific strength, elastic modulus and fracture toughness. These properties are highly dependent on the materials microstructure, i.e. texture, dislocation density, dislocation slip system activity. Therefore in order to be able to predict features of the materials and also to design materials with certain properties, a fundamental understanding of the deformation process in terms of microstructural parameters is critical [1].

The microstructural details can be obtained by using direct methods, such as transmission electron microscopy (TEM) techniques or by indirect methods, such as X-ray diffraction (XRD) or neutrons techniques. TEM methods reveal microstructural information over very small areas of the samples, which in turn raise issues of how representative are

* Corresponding author. Tel./fax: +1 404 385 6718.
*E-mail address:* iuliana.cernatescu@mse.gatech.edu (I.C. Dragomir).

1044-5803/$ - see front matter © 2005 Elsevier Inc. All rights reserved.
doi:10.1016/j.matchar.2005.03.002

the TEM microstructure parameters to the microstructure of the entire sample. On the other hand, XRD and neutron diffraction methods sample a large volume of the sample, which in turn provides an average representation of the studied material's microstructure. Moreover those experimental techniques are complementary. However, it should be noted that the sample preparation procedure required for TEM studies could modify the original microstructure of the studied material.

In recent years X-ray Peak Profile Analysis has been developed to such an extent that microstructural details, such as crystallite size distribution, defects density and types can be extracted from XRD pattern [2–5]. Deviations from perfect crystalline lattice affect the shape of the XRD lines, which no longer consists of narrow, symmetrical, delta-function like peaks, such as the diffraction lines given by an ideal powder diffraction pattern. Peak broadening is caused by crystallite smallness, lattice defects, stress gradients and/or chemical heterogeneities. X-ray line broadening exhibits an anisotropic behavior when dislocations are present in material. The anisotropic X-ray line broadening effect can be seen from the fact that neither the FWHM nor the integral breadth, nor the Fourier coefficients of the diffraction profiles are monotonic functions of the diffraction vector or its square, i.e. $g$ or $g^2$, respectively. Heterogeneous dislocations densities such as the accumulation of excess dislocations of one sign within dislocations walls or sub-boundaries cause asymmetric X-ray line shape. This effect can be interpreted in terms of local variations of lattice parameter associated with local variation of residual long-range internal stresses [6]. In the special cases of single crystal or coarse-grained materials, theoretical models have been developed enabling the evaluation of dislocations wall-cell arrangements by using Line Profile Analysis [6–8]. Further more it has been shown by Barabash et al. in [9] that by using white-beam Laue micro-diffraction, detailed information can be obtained about the heterogeneous dislocation structures.

It polycrystalline material populated with dislocations, the anisotropic line broadening can be taken into account by using that the dislocation model of the mean square strain, $\langle \varepsilon_{g,L}^2 \rangle$, (where $L$ is the Fourier length [10,11] and $\varepsilon_g$ is the distortion tensor component in the direction of the diffraction vector, $g$) [10]. In this model the dislocations are assumed to have a restrictedly random distribution within a region defined by $R_e$, the effective outer cut-off radius [10]. Here the anisotropic effect can be summarized in the average contrast factors, $C$, which depends on the relative orientations of the line and Burgers vectors of dislocations and the diffraction vector [4,11–16]. The contrast factor of dislocations is a measure of the "visibility" of dislocations in the XRD experiments. Since, the contrast effect is mainly a characteristic of dislocations, the theoretical values of the contrast factors and those obtained from the profile evaluation enable the determination of the active dislocation slip system(s) in the studied sample [12–16].

In this work, we present the evolution of the dislocation densities and types obtained from the X-ray peak profile analysis in commercially pure alpha-titanium deformed by rolling at 268 °C for the following rolling reduction levels: 40%, 60% and 80%. The dislocation densities and the average contrast factor of dislocation for each sample were determined by using Multiple Whole Profile (MWP) fitting procedure [18]. As described in detail in [18] in this procedure, the interpretation of the strain broadening is based on the dislocation model of the mean square strain. Here we note that from the present evaluation procedure only the overall average of dislocations densities were obtained. The determination of the geometrically necessary dislocations density would involve measurements of the Rocking-curves, however, this was not the goal of the present research [17]. The X-ray Peak Profile Analysis results show that: (I) the $\langle a \rangle$ type of dislocation predominates at all deformation levels investigated here; (II) the percentage of $\langle c+a \rangle$ type of dislocations are significant at the initial 40% reduction and becomes marginal at higher reduction rates; (III) the presence of $\langle c \rangle$ type of dislocation is minimal during the whole deformation range studied here. It was also established that the dislocation density slightly increases as the reduction degree increases. Further it is shown that the changes in Burgers Vector Population during the rolling deformation are in good agreement with the texture evolution.

## 2. X-ray peak profile analysis from MWP and methodology for determining Burgers Vector Populations

It is well known that the Fourier coefficients of the physical profiles can be written as a multiplication of the Fourier coefficients corresponding to the size and distortion effect [16]:

$$A_L = A_L^S A_L^D = A_L^S \exp\left[-2\pi^2 L^2 g^2 \langle \varepsilon_{g,L^2} \rangle\right], \quad (1)$$

where S and D indicate size and distortion, $g$ is the absolute value of the diffraction vector, $\langle \varepsilon_{g,L}^2 \rangle$ is the mean square strain and $L$ is the Fourier variable. As shown in [10,11,19] in a dislocated crystal, the mean square strain can be written in terms of dislocation density and the strain anisotropy, which can be taken into account by introducing the dislocation contrast factors, $\langle \varepsilon_{g,L^2} \rangle \cong \left(\rho \overline{Cb^2}/4\pi\right) f(\eta)$, where $\rho$ and $b$ are the density and the modulus of the Burgers vectors of dislocations and $\overline{Cb^2}$ is the average contrast factor of the dislocations present in the sample multiplied by the square of the dislocations Burgers vector. $f(\eta)$-function is the Wilkens function, where $\eta = L/R_e$ and $R_e$ is the effective outer cut-off radius of dislocations [10].

As shown in [12–15], contrast effect of dislocations depends not only on the material, but also on the relative orientation of the diffraction vector, $g$, line vector, $l$, and Burgers vector, $b$. Due to this in the case of hexagonal crystals, the three major slip systems, basal, prismatic and pyramidal, have to be divided in the 11 sub-slip systems by taking into account the different slip system types and the dislocation character (i.e. edge or screw). These 11 sub-slip systems are illustrated in Fig. 1 and listed in Table 1. It has been shown in earlier studies that in the case of hexagonal crystals for a given sub-slip system, the average contrast factor of dislocation can be written as [15]:

$$\bar{C}_{hk\cdot l} = \bar{C}_{hk\cdot 0}\left[1 + q_1 x + q_2 x^2\right], \quad (2)$$

where $x = (2/3)(l/ga)^2$, $q_1$ and $q_2$ are parameters which depend on the elastic properties of the

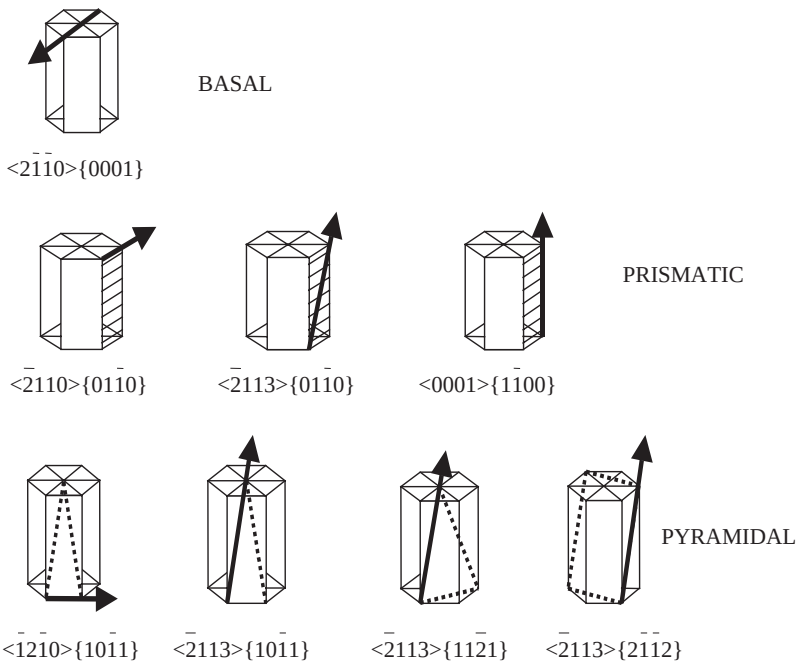


Fig. 1. The dislocation slip system in hexagonal crystal systems considered for the present study.

Table 1
The most common slip systems in hexagonal crystals

(a) Edge dislocations

| Major slip systems | Slip systems | Burgers vector | Slip plane | Burgers vector types |
|---|---|---|---|---|
| Basal | BE | $\langle 2-1-10\rangle$ | $\{0001\}$ | $a$ |
| Prismatic | PrE | $\langle -2110\rangle$ | $\{01-10\}$ | $a$ |
| | PrE2 | $\langle 0001\rangle$ | $\{01-10\}$ | $c$ |
| | PrE3 | $\langle -2113\rangle$ | $\{01-10\}$ | $c+a$ |
| Pyramidal | PyE | $\langle -12-10\rangle$ | $\{10-11\}$ | $a$ |
| | Py2E | $\langle -2113\rangle$ | $\{2-1-12\}$ | $c+a$ |
| | PyE3 | $\langle -2113\rangle$ | $\{11-21\}$ | $c+a$ |
| | PyE4 | $\langle -2113\rangle$ | $\{10-11\}$ | $c+a$ |

(b) Screw dislocations

| Slip systems | Burgers vector | Burgers vector types |
|---|---|---|
| S1 | $\langle 2-1-10\rangle$ | $a$ |
| S2 | $\langle -2113\rangle$ | $c+a$ |
| S3 | $\langle 0001\rangle$ | $c$ |

material, $\bar{C}_{hk\cdot 0}$ is the average contrast factor corresponding to the $hk\cdot 0$ type reflections, $a$ is the lattice constant in the basal plane, $g$ is the diffraction vector and $l$ is the last index of the $hk\cdot l$ reflection for which the $\bar{C}_{hk\cdot l}$ is evaluated. Eq. (2) is valid only when it can be assumed that within a sub-slip system, the dislocation can slip with the same probability in all directions permitted by the hexagonal crystal symmetry.

As it has been shown in [15] in the case of hexagonal crystal, the measured average $\overline{Cb^2}(m)$ characteristic to the examined sample can be written as follows:

$$\overline{Cb^2}^{(m)} = \sum_{i=1}^{N} f_i \bar{C}^{(i)} b_i^2, \tag{3}$$

where $N$ is the number of different activated sub-slip systems, $\bar{C}^{(i)}$ is the theoretical value of the average contrast factor corresponding to the $i$th sub-slip system and $f_i$ are the fractions of the particular sub-slip systems by which they contribute to the broadening of a specific reflection. On the left hand side of the Eq. (3), the $m$ superscript refers to the measurable strain anisotropy parameter, $\overline{Cb^2}$. For the hexagonal crystal structure, Eq. (3) can be written for the three fundamental Burgers vectors types defined in the hexagonal systems: $b_1=1/3\langle\bar{2}110\rangle$, $b_2=\langle 0001\rangle$, and $b_3=1/3\langle\bar{2}113\rangle$:

$$\overline{b^2 C_{hk\cdot l}}^{(m)} = b_1^2 \sum_{i=1}^{N\langle a\rangle} f_i \overline{C^{(i)}} + b_2^2 \sum_{j=1}^{N\langle c\rangle} f_i \overline{C^{(j)}} + b_3^2 \sum_{n=1}^{N\langle c+a\rangle} f_i \overline{C^{(n)}}, \tag{4}$$

where $N\langle a\rangle$, $N\langle c\rangle$ and $N\langle c+a\rangle$ are the numbers of sub-slip systems with the Burgers vector types $\langle a\rangle$, $\langle c\rangle$ or $\langle c+a\rangle$, respectively. The possibility of measuring $q_1$ and $q_2$ offers three independent equations and 11 unknowns. This means that Eq. (4) can give an exact solution only by making certain assumptions about the activated dislocation slip systems. In the present work it is assumed that a particular Burgers vector type has random (or uniform) distribution in the different slip systems. In this case Eq. (4) can be written:

$$\overline{b^2 C_{hk\cdot i}}^{(m)} = \sum_{i=1}^{3} h_i \bar{C}^{(i)} b_i^2, \tag{5}$$

where $h_i$ is the fraction of the dislocations population in the sample with the same Burgers vector, $b_i$. $C^{(i)}$ is the averaged contrast factor over the sub-slip systems, for the same Burgers vector type. Inserting Eq. (2) into Eq. (5), the following three equations are obtained:

$$q_1^{(m)} = \frac{1}{P} \sum_{i=1}^{3} h_i \bar{C}_{hk\cdot 0}^{(i)} b_i^2 q_1^{(i)}, q_2^{(m)} = \frac{1}{P} \sum_{i=1}^{3} h_i \bar{C}_{hk\cdot 0}^{(i)} b_i^2 q_2^{(i)}, \sum_{i=1}^{3} h_i = 1, \tag{6}$$

where $P = \sum_{i=1}^{3} h_i \bar{C}_{hk\cdot 0}^{(i)} b_i^2 = \overline{b^2 C_{hk\cdot 0}}^{(m)}$ and $0 \le h_i \le 1$. To solve Eq. (6), the numerically calculated values of $\bar{C}_{hk\cdot 0}$, $q_1$ and $q_2$ for all sub-slip systems are required. The theoretical values of $\bar{C}_{hk\cdot 0}$, $q_1$ and $q_2$ for the most common sub-slip systems were published previously in [15]. The contrast factor of dislocation for hexagonal crystals in elastic anisotropic and isotropic media has been treated by Kuzel and Klimanek [12–14].

The measured values of $q_1$ and $q_2$ parameters were obtained from the Multiple Whole Profile (MWP)

fitting procedure [18]. In this procedure the Fourier-transformed of multiple *hkl* reflections are fitted simultaneously by Eq. (1). Here, throughout the $q_1$ and $q_2$ parameters in Eq. (2), the dislocation contrast factor becomes a fitting parameter.

## 3. Experimental procedures

Titanium specimens were rolled at 268 °C to a reduction of 40%, 60% and 80%. A Lindberg/Blue model BF51800 electrical furnace was used to heat the samples. In order to obtain a homogeneous deformation, a step-size of 5% for reduction was applied. After each pass of 5%, the sample was immediately returned to the furnace for reheating and again deformed to an additional reduction of 5%. The procedure was repeated till the desired reduction level was achieved. After the final step the samples were cooled in air.

In order to remove the formed oxide layer before the X-ray diffraction experiments, each sample was chemically etched. The texture measurements were performed using a Philips X'Pert MPD, equipped with texture goniometer; using Cu $K_\alpha$ radiation, point source, 1-mm × 1-mm cross slit and 1-mm receiving slit. Five incomplete pole figures (0002), ($10\bar{1}1$), ($10\bar{1}2$), ($11\bar{2}0$) and ($10\bar{1}3$) were measured with step-size of 5° and 4 s/step. The data files from Philips were converted into raw archives, recognizable by Preferred Orientation Package-Los Alamos (PopLA), using PC-Texture 3.0. Orientation distribution functions and complete pole figures were calculated using the PopLA software.

The diffraction profiles necessary for the Peak Profile Analysis were measured using an Alpha-1 Panalytical Diffractometer set up in Bragg-Brentano geometry. Using a symmetrical incident beam Johansson monochromator, only the Kα1 component of Cu radiation was used. The profile data acquisition was done using a solid-state position-sensitive ultra-fast detector (X'Celerator/Panalytical). In order to reduce the instrumental effect, a divergent slit of ¼° and soller slits of 0.02 rad. were used on incident beam path. On the diffracted beam path, 0.02 rad. soller slits and a 5.0-mm anti-scattering slit were used. A mask of 5 mm was inserted to adjust the size of the probing X-ray spot. For each sample the following reflections were measured: 0002, $10\bar{1}1$, $10\bar{1}2$, $11\bar{2}0$, $10\bar{1}0$, $10\bar{1}3$ and 0004. The instrumental broadening was measured using NIST SMR660a ($LaB_6$). As the measured profile is a convolution of the physical with the instrumental profile, the Stokes correction [20] based on the Fourier transforms of the profiles was used to determine the physical line profiles. Background and instrumental profile correction were done with the MKDAT program described elsewhere [18].

## 4. Results and discussion

In the present work the evaluation of the X-ray diffraction profiles was carried out by using the Multiple Whole-Profile (MWP) fitting procedure. Here the Fourier coefficients of the measured physical profiles are fit all at once by the product of the theoretical functions for size ($A^S$) and strain caused by distortion in the crystal ($A^D$) broadening, as shown in Eq. (1). In this evaluation, it is assumed that the peak broadening is caused by the smallness of the coherently scattering domains and by strain effect arising from the presence of dislocations. As it has been shown in [18] for case of hexagonal crystals, the MWP fitting procedure enables the evaluation of six microstructure parameters: (a) the dislocation density and arrangement parameter, $\rho$ and $M$. $M$ is defined by Wilkens as the dislocation arrangement parameter in the Wilkens function [10], the value of $M$ gives the strength of the dipole character of dislocations: the higher the value of $M$, the weaker the dipole character and the screening of the displacement fields of dislocations [10]. (b) The median and the variance, $m$ and σ, in the size part of the profiles and (c) $q_1$ and $q_2$ the parameters of the dislocation contrast factors as shown in Eq. (2). Details of the MWP method can be found in [18]. In the present study the effect of crystallite size was found to tend to infinity. This is due to the fact that the coherent domain is greater than few μm. In this case the effect of size broadening is insignificant compared with the distortion effect.

As shown in Section 2 the presence of crystallographic texture complicates the interpretation of peak broadening observations. In an attempt to emulate a random polycrystalline specimen, the strongest diffraction peaks from the three different faces of the orthogonal sample were mixed to form a full

Table 2
Dislocation densities and arrangement parameter, $M$, obtained from MWP evaluation for Ti samples deformed at different reduction levels

| Rolling reduction [%] | 40% reduction | 60% reduction | 80% reduction |
|---|---|---|---|
| $M$ | 2.9 | 1.7 | 1.1 |
| $\rho$ [1/cm$^2$] | $5\times10^{10}\pm5\%$ | $8\times10^{10}\pm10\%$ | $10^{11}\pm7\%$ |

diffraction pattern and used in the MWP evaluation [21,22]. These mixed patterns were then used in the MWP evaluation. The results for the dislocation densities and the arrangement parameter, $M$, are listed in Table 2 for the titanium specimens deformed at 40%, 60% and 80% reduction levels. The errors of the dislocations densities listed in the table are calculated from the covariance matrix in the refinement. It can be observed from Table 2 that the increment of ñ is small in accordance with a dynamic recovery effect, where dislocation annihilation may occur due to the high deformation temperature. The values of $M$ in Table 2 indicate that the dislocations in the titanium samples studied here exhibit a weak dipole character.

The $h_i$ fractions of dislocation density with the three Burgers vector types, $\langle a\rangle$, $\langle c\rangle$ and $\langle c+a\rangle$, are shown as a function of deformation level in Fig. 2. The results show that: (I) in the specimen deformed at 40% the $\langle c+a\rangle$ and $\langle a\rangle$ dislocations type are dominating the dislocation population present in the sample; (II) at higher deformation levels $\langle a\rangle$ type is the dominant dislocation type and the presence of $\langle c+a\rangle$ dislocation decrease; (III) at all deformation levels the fraction of $\langle c\rangle$ dislocations type is marginal. The activity of $\langle c+a\rangle$ dislocations plays an important role in dynamic recovery. Screw dislocations of $\langle c+a\rangle$ type can move to the next slip planes by double cross slip followed by dislocation annihilation. Dislocations with $\mathbf{b}=\langle 0001\rangle$ Burgers vector are sessile, thus its presence can be seen practically unchanged in the deformation range studied here [23,24]. The results presented here are in good agreement with previous works, where the $\langle a\rangle$ dislocation types are most frequently observed in deformed Ti and $\langle c+a\rangle$ and $\langle c\rangle$ types were also reported from extensive TEM studies [23,24].

Fig. 3 illustrates the (0002) and (11–20) Bragg reflections profiles for all deformations levels studied

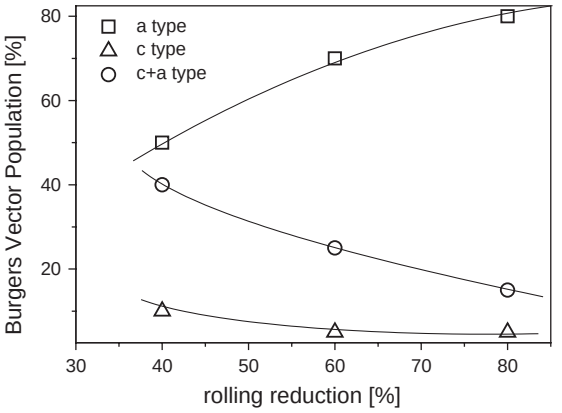


Fig. 2. The $h_i$ fractions of the three fundamental Burgers vector types, $\langle a\rangle$, $\langle c\rangle$ and $\langle c+a\rangle$, as a function of rolling reduction. Note that in the figure the solutions to Eq. (6), the $h_i$ fractions, were transformed in percentages.

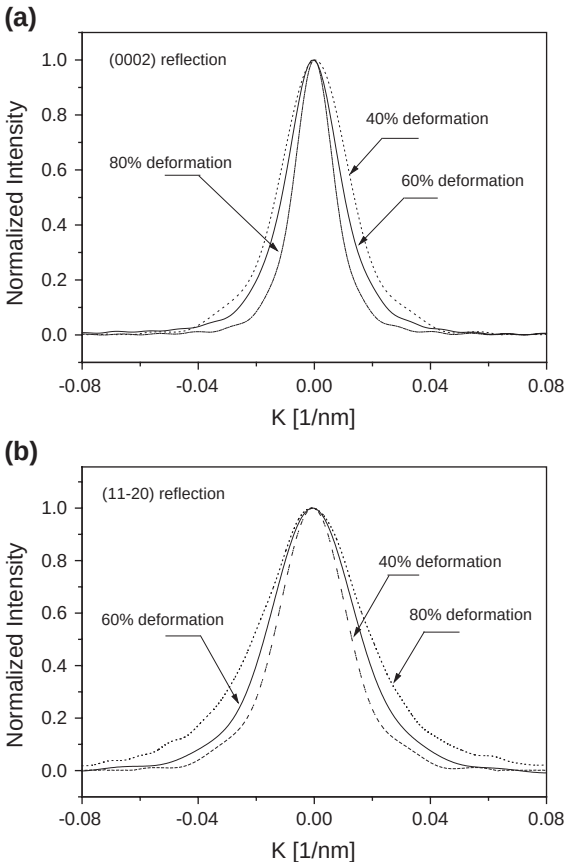


Fig. 3. The line profiles of (a) (11–20) and (b) (0002) Bragg reflections for different deformations levels. On the $x$-axes $K$ is given by $K=2\sin\theta/\lambda$, where $\theta$ is the Bragg angle and $\lambda$ is the wavelength of the used radiation.

here. The difference in broadening is due to the difference in the dislocations types accumulated in each sample. From Fig. 3(a) it can be observed that the broadening of the (0002) reflections is decreasing as the deformation increases. However, Fig. 3(b) shows that the breadth of (11–20) reflections increases as the deformation increases. The two figures are an illustration of the different contrast effect due to different types of dislocations and are an indication that the content of dislocations with $\langle a \rangle$ Burgers vector type increases as the deformations process to higher levels.

In accordance with the dislocations slip directions, $\langle a \rangle$, $\langle c \rangle$ and $\langle c+a \rangle$, (0001), ($\bar{2}$110) and ($\bar{2}$113) pole figures were measured for each Ti sample studied here. The pole figures of (0001), ($\bar{2}$110) and ($\bar{2}$113) at different deformation status are illustrated in Fig. 4(a–d). The as received material exhibits a weak texture. Fig. 4(a) shows that $\langle 0001 \rangle$ directions of most of the crystals are distributed on the plane of ND (normal direction)–RD (rolling direction). When the sample is rolled to a strain of 40%, $\langle 0001 \rangle$ directions of the crystals move close to ND, as shown in Fig. 4(b). The same trend is also observed in Fig. 4(c) for the sample

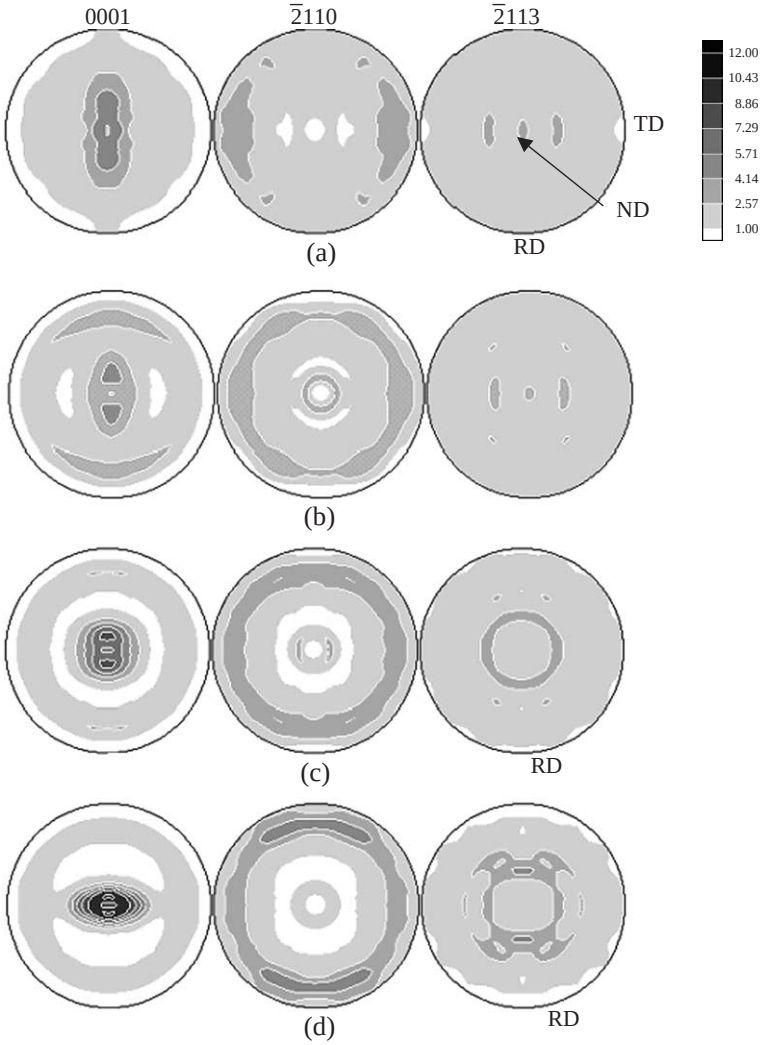


Fig. 4. $\langle \bar{2}110 \rangle$, $\langle 0001 \rangle$ and $\langle \bar{2}113 \rangle$ pole figures of alpha-titanium at a rolling reduction of (a) 0%, (b) 40% (c) 60%, (d) 80%, respectively.

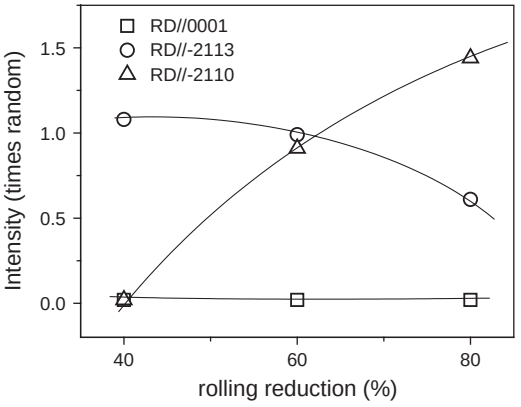


Fig. 5. Evolution of intensities of components with RD//$\bar{2}110$, RD//0001 and RD//$\bar{2}113$, respectively, during rolling reduction.

rolled to a strain of 60%. In Fig. 4(d) the split from the ND direction becomes smaller at a higher strain of 80%. Comparing with $\langle 0001\rangle$, the evolution of $\langle\bar{2}110\rangle$ is not so complicated. The initial distribution of $\langle\bar{2}110\rangle$ is random. At a strain of 40%, $\langle\bar{2}110\rangle$ becomes oriented along the plane of RD–TD (transversal direction). At higher deformation rates $\langle\bar{2}110\rangle$ become concentrated close to RD, but 5° away. This corresponds to the split shown in the (0001) pole figures. The (0001) pole figures and ($\bar{2}110$) pole figures verify that the $\langle a\rangle$ type of slip is dominant during the rolling process. The ($\bar{2}113$) pole figures in Fig. 4 show that the number of crystals with $\langle\bar{2}113\rangle$ parallel to RD decreases with the increase of rolling strain. This is further demonstrated in Fig. 5, which shows the evolution pattern of the distribution density of crystals whose $\langle 0001\rangle$, $\langle\bar{2}110\rangle$ and $\langle\bar{2}113\rangle$ are parallel to the RD. It can be observed from Fig. 5 that the distribution density of the RD//$\langle\bar{2}110\rangle$ increases with the strain, while the RD//$\langle\bar{2}113\rangle$ decreases and the RD//$\langle 0001\rangle$ is always close to zero. This is in good correlation with the Burgers Vector Population results, which show that the density of $\langle a\rangle$ type of dislocations increases, while the density of $\langle c+a\rangle$ type of dislocations decreases and $\langle c\rangle$ type remains at very low values during the whole rolling process.

## 5. Conclusions

By using Peak Profile Analysis methods the evolution of dislocation density and the Burgers Vector Population has been evaluated as a function of reduction in titanium deformed by rolling at 268 °C. It was found that the $\langle a\rangle$ types of dislocations are dominating the whole deformation range studied here. The percentage of $\langle c+a\rangle$ dislocation type is present significantly at 40% reduction rate, but decreases as the deformation proceeds to higher values. The presence of $\langle c\rangle$ dislocation type is minimal during the whole deformation process. The X-ray Peak Profile Analysis results are in good correlation with the texture evolution studies presented here.

## Acknowledgements

We gratefully acknowledge the support of Panalytical Inc.

## References

[1] Picu RC, Majorell A. Mechanical behavior of Ti–6Al–4V at high and moderate temperatures: Part II. Constitutive modeling. Mater Sci Eng, A Struct Mater: Prop Microstruct Process 2002;326:306–16.
[2] Tian HH, Atzmon M. Comparison of X-ray analysis methods used to determine the grain size and strain in nanocrystalline materials. Philos Mag 1999;79(8):1769–86.
[3] Kamminga JD, Delhez R. Calculation of diffraction line profiles from specimens with dislocations. A comparison of analytical models with computer simulations. J Appl Crystallogr 2000;33:1122–7.
[4] Ungár T, Borbély A. The effect of dislocation contrast on X-ray line broadening: a new approach to line profile analysis. Appl Phys Lett 1996;69:3173–5.
[5] Scardi P, Leoni M. Whole powder pattern modelling. Theory and applications. In: Mittemeijer EJ, Scardi P, editors. Diffraction analysis of the microstructure of materials. Berlin: Springer; 2004. p. 51–91.
[6] Ungar T, Mughrabi H, Wilkens M, Hilscher A. Long-range internal stresses and asymmetric X-ray line-broadening in tensile-deformed [001]-oriented copper single crystals: the correction of an erratum. Philos Mag, A 1991;64(2):495–6.
[7] Groma I, Monnet G. Analysis of asymmetric broadening of X-ray diffraction peak profiles caused by randomly distributed polarized dislocation dipoles and dislocation walls. J Appl Crystallogr 2002;35(5):589–93.
[8] Ungar T, Biermann H, Mughrabi H. Dislocation distributions as seen by X-ray line profiles. Mater Sci Eng, A Struct Mater: Prop Microstruct Process 1993;A164(1–2):175–9.
[9] Barabash RI, Ice GE, Larson BC, Yang W. Application of white X-ray microbeams for the analysis of dislocation structures. Rev Sci Instrum 2002;73(3 Pt. 2):1652–4.

[10] Wilkens M. The determination of density and distribution of dislocations in deformed single crystals from broadened X-ray diffraction profiles. Phys Status Solidi, A Appl Res 1970;2: 359–70.
[11] Wilkens M. Fundamental aspects of dislocation theory. In: Simmons JA, De Witt R, Bullough R, editors. NBS Spec Publ, vol. 317 (2). 1970. p. 1195–221.
[12] Klimanek P, Kuzel Jr R. X-ray diffraction line broadening due to dislocations in non-cubic materials: I. General considerations and the case of elastic isotropy applied to hexagonal crystals. J Appl Crystallogr 1988;21:59–66.
[13] Kuzel Jr R, Klimanek P. X-ray diffraction line broadening due to dislocations in non-cubic materials: II. The case of elastic anisotropy applied to hexagonal crystals. J Appl Crystallogr 1988;21:363–8.
[14] Kuzel Jr R, Klimanek P. X-ray diffraction line broadening due to dislocations in non-cubic materials: III. Experimental results for plastically deformed zirconium. J Appl Crystallogr 1989; 22:299–307.
[15] Dragomir IC, Ungár T. Contrast factors of dislocations in the hexagonal crystal system. J Appl Crystallogr 2002;35:556–64.
[16] Ungár T, Tichy G. The effect of dislocation contrast on X-ray line profiles in untextured polycrystals. Phys Status Solidi 1999;171:425–34.
[17] May C, Klimanek P. Integrated X-ray substructure analysis of plastically deformed beryllium single crystals. Nuovo Cim Soc Ital Fis, D 1997;19(2–4):591–8.
[18] Ribárik G, Ungár T, Gubicza J. MWP-fit: a program for multiple whole-profile fitting of diffraction peak profiles by ab initio theoretical functions. J Appl Crystallogr 2001;34:669–76.
[19] Krivoglaz MA. X-ray and neutron diffraction in nonideal crystals. Berlin: Springer-Verlag; 1996. p. 358.
[20] Stokes AR, Wilson AJC. The diffraction of X-rays by distorted crystal aggregates: I. Proc Phys Soc Lond 1944;56:174–81.
[21] Glavicic MG, Salem AA, Semiatin SL. X-ray line-broadening analysis of deformation mechanisms during rolling of commercial-purity titanium. Acta Mater 2004;52(3):647–55.
[22] Gubicza J, Dragomir IC, Ribárik G, Baik SC, Zhu YT, Valiev RZ, et al. Dislocation structure and crystallite size distribution in plastically deformed Ti determined by X-ray peak profile analysis. Z Metkd 2003;94:1185–8.
[23] Jones IP, Hutchinson WB. Stress-state dependence of slip in titanium–6Al–4V and other hcp metals. Acta Metal 1982;29: 951–68.
[24] Song SG, Gray III GT. Structural interpretation of the nucleation and growth of deformation twins in Zr and Ti: II. TEM study of twin morphology and defect reactions during twinning. Acta Mater 1995;43:2339–50.